Catalysis Science & Technology

Entropic influence on the generation of Fe(IV)O species at mononuclear Fe(II) sites in metal-organic frameworks

Journal:	*Catalysis Science & Technology*
Manuscript ID	CY-ART-03-2023-000392.R1
Article Type:	Paper
Date Submitted by the Author:	09-Aug-2023
Complete List of Authors:	Saiz, Fernan; ALBA synchroton, Scientific Data Engineering Bernasconi, Leonardo; University of Pittsburgh, Center for Scientific Computing

Journal Name

ARTICLE TYPE

Cite this: DOI: 00.0000/xxxxxxxxxx

Entropic influence on the generation of Fe(IV)O species at mononuclear Fe(II) sites in metal-organic frameworks

Fernan Saiz [a] and Leonardo Bernasconi [b]

Received Date
Accepted Date

DOI: 00.0000/xxxxxxxxxx

We study the oxidation of mononuclear Fe(II) centers in the metal-organic framework MOF-74 in the presence of nitric oxide (NO), nitrogen dioxide (NO_2), nitrous oxide (N_2O), dinitrous dioxide (N_2O_2), oxygen (O_2), ozone (O_3), and hydrogen peroxide (H_2O_2) using static density-functional theory calculations and *ab initio* molecular dynamics simulations. We examine the effect of reaction entropies at room temperature on the Fe(II) oxidation barriers for these species. Singlet N_2O, O_2 and H_2O_2 exhibit large positive entropic contributions, which reduce the free energy barrier at room temperature compared to the enthalpy barriers. By contrast, large negative entropies are observed in the case of NO_2 and O_3, which indicate that the reactivity of these species decreases with temperature. We discuss the role of entropic effects on the mechanisms and energetics of the reactions examined.

1 Introduction

The use of metal-organic frameworks (MOFs) in heterogeneous catalytic processes for the oxidation of saturated substrates has been emerging in recent years as an alternative to more traditional chemical routes based on solution chemistry.[1] MOFs are porous materials composed of molecular blocks, which offer the possibility of adding chemically active ligands or metallic centers. The addition of these species makes it possible to tailor catalytic sites for application in fine chemistry and, potentially, industrial processes.[2] One of the most sought after applications in this field is the hydroxylation of light alkanes, such as methane or ethane (which constitute 94.7 % and 4.2 % of natural gas), to reduce the transport costs from production sites to consumption areas. For instance, the direct transportation of methane can be done by converting this gas into liquid species such as dimethyl ether, formaldehyde, acetic acid, or liquid fuels, using Fischer-Tropsch catalytic processes. Methane can also be oxidised to methanol using several multi-step industrial processes.[3]

In addition to these traditional processes for hydrocarbon activation, several solid-state catalysts have recently been investigated, such as MOFs or zeolites. An interesting class of these compounds that have been shown to be promising in this field are catalysts based on high-valent Fe(IV)oxo species supported by a solid-state host. Fe(IV)oxo species are known to play central roles in biological processes, including aerobic respiration, catabolism and the *in vivo* oxidation of hydrocarbons.[4–15] The origin of the extraordinary reactivity of the Fe(IV)oxo species has also been the subject of extensive theoretical and computational work.[12–14,16–19], but only a limited number of computational studies have been published so far to investigate the oxidation of e.g. methane and ethane[13,20–25] in MOFs, of benzene on graphene[26], of CO with N_2O through an oriented external electric field in the MOF Fe3(btc)2,[27] and of methane in zeolites.[28–32] Solid-state Fe(IV)O systems have been also investigated for their potential to store methane in the case of MOF74,[33] NO adsorption in Al-rich beta zeolites[34] and in MOFs,[35] NO and N_2O reduction by NH_3 within the framework of the zeolite Fe-BEA,[36–38] and the decomposition of nitrous oxide (N_2O) in the zeolites Fe-FER, Fe-BEA, and Fe-MFI.[39,40]

Whereas much is known about the generation and reactivity of Fe(IV)oxo in biochemistry, biomimetic chemistry and solution chemistry,[41–47] the study of these species supported by inorganic crystalline materials is still in its infancy. In particular, the generation of a ferryl group in the solid state and its regeneration as this species is consumed during a catalytic oxidation process, remain to be addressed. In the specific case of MOFs, the generation of active sites is an active area of research since the use of these materials in large-scale industrial processes depends crucially on it.[48] Although a mechanism for the production of Fe(IV)oxo by reduction of H_2O_2 in the solid state has been proposed,[49] the study of oxidants alternative to H_2O_2 has remained a relatively minor area of computational research. Conversely, an extensive literature exists on the ability of Fe(IV)oxo to act as a catalyst for C-H activation in MOFs.[20,21,50–52] Thus, understanding the mechanistic details of the Fe(IV)oxo generation is a crucial component in

[a] *ALBA Synchrotron, Carrer de la Llum 2-26, Cerdanyola del Valles 08290, Spain, E-mail: fsaiz@cells.es*
[b] *Center for Research Computing, University of Pittsburgh, 312 Schenley Place, 4420 Bayard Street, Pittsburgh, PA 15260, United States of America, E-mail: leb140@pitt.edu*

models of the catalytic activity of this species in MOFs.

In this work we explore computationally the ability of nitric oxide (NO) and dioxide (NO_2), nitrous oxide (N_2O), dinitrous dioxide (N_2O_2), oxygen (O_2), ozone (O_3) and hydrogen peroxide (H_2O_2) to oxidize *mononuclear* Fe(II) metal centers supported by a MOF-74 framework to Fe(IV)O species. We consider these oxidants because some of them are currently used in experimental or computational investigations of the potential of MOFs and zeolites as catalyst for conversion of methane into methanol. For example, this conversion has been also experimentally characterised in the case of NO[53], O_2 and NO_x[54], H_2O_2[55–57]. Specifically, NO has been recently proposed to react with Fe dimers in Fe(II) Pyrazolate MOF to produce nitrous oxide[58] and also with substituted β-diketonates (Fe/acacX) complexes to yield high-spin (S = 3/2) FeNO[59]. Other molecules, such as N_2O, have been used to activate Fe(II) sites by oxygen-transfer for the low-temperature methane hydroxylation in iron-containing zeolites[60] and MOFs[24,61], suggesting that these species are sufficiently reactive to convert Fe(II) to Fe(IV)O.

We use first-principles calculations to study the mechanisms that are thermodynamically favourable in the conversion of Fe(II) into Fe(IV)O centres upon the adsorption of the species mentioned above. These reactions are studied at 0 K and at room temperature using two methods. In the first method, which we will refer to as the *static* approach, we calculate the reaction enthalpy ΔH using a series of consecutive constrained geometry optimisations in which the adsorbent is gradually displaced toward a Fe(II) site with a given angle of attack. The second method uses *ab initio* molecular dynamics (AIMD) to model the approach of the oxidant species whilst sampling a very large number of angles of approach, which allows estimating reaction free energies ΔG at room temperature. From the enthalpies and free energies, we then compute the associated reaction entropies ΔS. At variance with static calculations followed by thermal analysis, our AIMD calculations also account for anharmonic vibrational effects.

After this introduction, this manuscript is organised as follows. Section 2 describes the details of the density-functional theory (DFT) approaches used in the static and AIMD method to calculate reaction barriers. In Section 3, we present the mechanisms involved in the activation of the Fe(II) to Fe(IV)Ooxo for all adsorbents as well as their associated reaction enthalpies and free energies. We evaluate the differences between the static and dynamics approaches. Finally, in Section 4 we present our conclusions and the implications of this work.

2 Simulation Methods

The initial structure of Fe(II)O/MOF-74 used in our calculations is derived from crystallographic data for acetylene/MOF-74[10] deposited in the Cambridge Crystallographic Database[62], which is modified using the Materials Studio suite package[63] as follows. We replace the acetylene molecule present in the original structure (SARGID 866357) with an oxygen atom O(oxo), at a distance of 1.68 Å from the Fe atom, which is slightly larger than the typical Fe(IV)–O(oxo) distances determined for gas-phase complexes (1.60–1.62 Å).[64] We then optimise the atomic positions with the COMPASS2 force field. After optimisation, the Fe(IV)–O(oxo) bond length decreases to 1.65 Å.

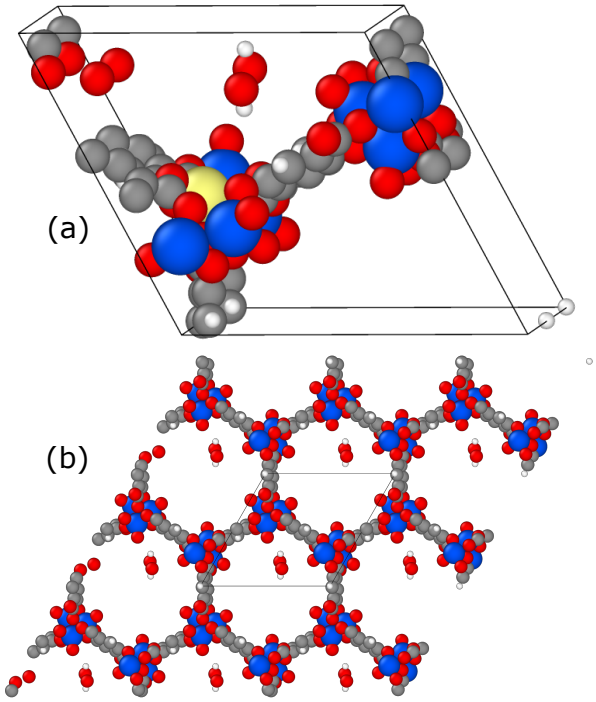

Fig. 1 Representation of the periodic Fe(II)/MOF-74 cavity with a hydrogen peroxide molecule (a) inside the pore used in the CP2k calculations and its replicated cell (b). Fe atoms are blue (except for the active Fe(II) atom, which is yellow), O atoms red, C atoms grey, and H atoms white. These views are generated with the OVITO package[65].

We use the CP2k/QUICKSTEP code[66,67] to calculate the associated reaction enthalpy using a static approach based on running a set of consecutive constrained geometry optimizations and the free energies of reaction using AIMD simulations. Both types of calculations use standard GTH pseudopotentials[68,69], double-ζ basis sets with polarisation functions (DZVP-MOLOPT-SR-GTH), and spin-polarised solutions at the range-separated hybrid DFT level of theory HSE06[70]. According to previous work, have ange-separated hybrid functional such as sc-BLYP[71] provide accuracy in reaction barriers for this system comparable to global hybrid functionals, like B3LYP.[72–74] The use of hybrid exchange in the density functional is also required to remove spurious self-interaction effects responsible for anomalous reaction profiles and unphysical reaction energy barriers.[50,51] Although the use of HSE06 is computationally very demanding (each AIMD step requiring around 85 seconds with 144 MPI processes on Intel Gold 6126 CPUs) it is required to obtain accurate reaction (free) energy barriers, which are crucial for identifying the reaction's rate-determining step (abstraction, rebound or detachment).

Van der Waals interactions are estimated using Grimme's DFT-D3 correction[75]. We use the default tolerance for the charge density residual of 1 x 10^{-5} e^-/Bohr^3 for the self-consistent solution of the Kohn-Sham equations with an energy cut-off of 500 Ry, which is justified in Figure S1 in the Supplementary Information.

All CP2k calculations are carried out in the Γ point approximation on a super-cell containing 119 atoms, with dimensions $a = 13.90$ Å and $b = c = 15.14$ Å, $\alpha = 117.70°$ and $\beta = \gamma = 98.79°$. This supercell contains 12 Fe atoms and, based on our previous work,[51] we assume that all of them are in a quintet spin state and that they are magnetically uncoupled. Indeed, preliminary calculations show that this state has a lower total energy than the triplet's (by 11.01 eV) and singlet's (by 17.97 eV) when the methane molecule is far away from the Fe(IV)Ooxo reactive site. These HSE06 results are in agreement with our previous findings on generalized gradient approximations (GGAs) and other hybrid levels of theory.[51,52] These findings allows us to set different spin multiplicities on our CP2k/HSE06 simulations to adjust the configuration of the oxidants examined here.

Enthalpies of reaction are estimated with the static approach, in which an oxygen atom within the reactant molecule in the abstraction step (or the radical in the radical rebound step) is gradually displaced towards the Fe(II) atom (or the Fe(III)O complex) using small steps of *ca.* 0.1 Å. In each of these steps, the geometry of the system is optimized while constraining the position of the Fe(II) and one O of the reactant molecule. The optimization is considered to be converged when all the atomic forces are below 0.05 eV/Å. The enthalpy is then estimated from the difference between the minimum and the maximum total energies for all constrained distances.

Free-energy reaction barriers are estimated using the potential of mean force (PMF) method[76,77] from constrained AIMD NVT simulations carried out at constant volume and at a temperature of 300 K. A timestep of 0.5 fs is used to integrate the equations of motion and a Nosé-Hoover thermostat[78,79] with a chain time constant of 1 ps is used to control the temperature. In the initial abstraction step, we set the constraint length ξ as the distance between the Fe(II) atom and one of the O atoms for all adsorbed species. For some of the reactant species considered, further reaction steps are required, *e.g.* the detachment of the product after Fe(IV)O is formed. In these cases, the separation between O(oxo) and one of the atoms of the departing molecule are constrained. For all these steps, we carry out a series of AIMD simulations, in which ξ is progressively decreased or increased, depending on the process, and for each value of the constrained distance, ξ_i, we compute the mean force of the constraint $f(\xi_i)$ from an unbiased time averaged value of $\lambda(\xi_i)$, where $\lambda(\xi_i)$ is the average value of the Lagrangian multiplier $\lambda(\xi_i)$ which is used to maintain the constraint to its fixed value[76,77,80]:

$$f(\xi_i) - f_0 = \langle \lambda(\xi_i) \rangle - \frac{2k_B T}{\xi_i}, \quad (1)$$

where k_B = 1.38 x 10^{-23} J/K, T = 300 K, and f_0 is the value of $f(\xi_i)$ for the initial simulation. The free energies associated with each process are given by

$$\Delta G = -\int_{\xi_0}^{\xi_N} f(\xi')d\xi'. \quad (2)$$

For the calculation of free energy barriers, ξ_N is chosen as the value of ξ closest to a free energy maximum. Finally, once the values of ΔH and ΔG are found, we determine the associated entropy S for any reaction step using the classical expression

$$\Delta S = \frac{\Delta H - \Delta G}{T}. \quad (3)$$

3 Results and Discussion

3.1 Nitric oxide

We begin our analysis by studying whether the adsorption of one NO molecule at a MOF-74/Fe(II) centre can lead to the formation of a Fe(IV)O species. NO and NO_2 are highly unusual molecules because they are free radicals that are sufficiently stable to be stored for long periods at ambient conditions. Thus, they have served to track the reactivity in multiple heterogeneous processes such as the production of N_2O from the reduction of NO on aquated Fe(II),[81,82] and the interactions of NO with tetrathiolato Fe(II) complexes Fe(II).[83] Even if these studies suggest that NO can bind to Fe(II), it remains unclear how this radical influences the oxidation state of Fe(II). Hence, we consider here two spin states, one with total spin multiplicity $S = 52$, corresponding to an NO molecule in its quartet configuration, and $S = 50$ for the molecule doublet state. In all cases, we assume that the Fe(II) centres are in a quintet configuration, consistent with previous work. We use these spin configurations in both the static and dynamic approach, where we fix the distance between Fe(II) and the NO's oxygen to a constant value, which decreases till distances of *ca.* 1.6 Å are reached.

Figure 2(a)-(b) shows the enthalpy profile obtained from constrained geometry optimizations for doublet and quartet NO. For both spin states, the static approach indicates a quasi-monotonic increase of the energy $H^{S=2}_{NO,ads}$ with decreasing Fe(II)-O separation. For separations larger than 2.5 Å, the DFT total and Van der Waals energy curves exhibit slight offsets, owing to the reorientation of the molecule as it approaches the Fe(II) centre. For separations shorter than 2.5 Å, the enthalpy of the quartet increases to reach a maximum of 75.19 kJ/mol at 1.88 Å, after which it slightly decreases to 51.28 kJ/mol at 1.80 Å. This feature corresponds to a spatial readjustment of the NO molecule to reorient its bond axis as it approaches the Fe(II) site, which also coincides with some other made by Fe(II) neighbours in the MOF structure as shown by Figures S2(a) and (b). These enthalpy profiles indicate that, at 0 K, NO exhibits no tendency to react with the Fe(II) centre, irrespectively of the oxidant's spin state, as the total energy curves fail to show a well-defined minimum at the characteristic Fe(IV)O bond distance (1.65-1.70 Å[50–52]).

We study the same processes at 298 K using AIMD simulations. The corresponding mean forces of constraint and integrated free energies are shown in Figure 2(c) and (d). In the case of the quartet, the mean force of the Fe-O constraint indicates the existence of a moderate repulsion at 2.75 Å, which is absent for the doublet. We hypothesize that this repulsion for the quartet appears due to the stronger interaction between the electrons of the outmost 3d orbitals of Fe(II) and those of the NO that with the same. This interaction can be interpreted in terms of an off-site exchange repulsion,[84,85] promoted by the relatively high spin moments on Fe and NO. Furthermore, we note that the mean force of the con-

straint is never negative in the quartet state, which indicates that no reaction is taking place leading to the formation of a Fe-O bond. By contrast, the doublet state shows a modestly negative (attractive) mean force between Fe and O within the separation range 2.5-1.8 Å. We can therefore estimate a free energy of reaction of 98.27 kJ/mol in this case, by integrating the mean force to bond distances of 1.63 Å, as shown by Fig. 2(c). Despite the substantial free energy required for this process to occur, we notice that finite temperature effects tend to promote the initial interaction of Fe(II) and NO, which leads to the formation of an Fe(III)O–N species. However, even at room temperature, we do not observe the breaking of the N-O bond (see Figure S3), which suggests that the full oxidation of Fe(II) to Fe(IV)O is not taking place. Based on these findings, we can conclude that NO does not react at 0 K. The doublet state at room temperature appears to be more reactive, but the oxidation of Fe(II) does not lead to the formation of Fe(IV)O, but only to the partial oxidation of Fe(II) to Fe(III).

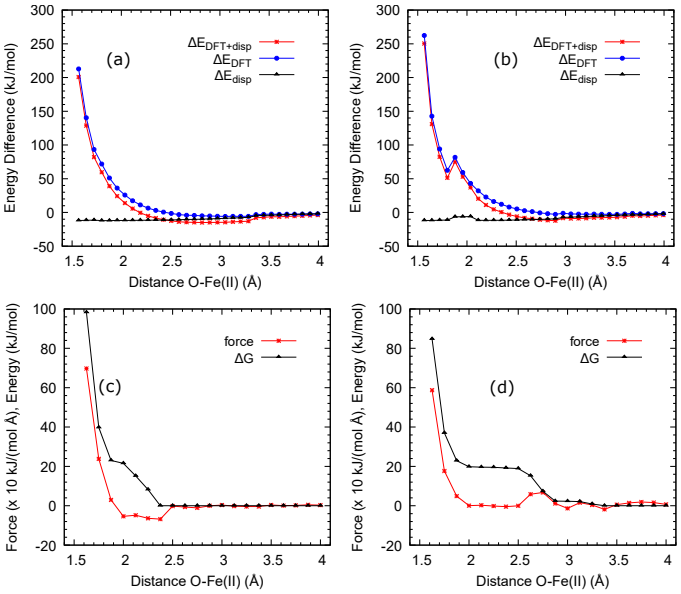

Fig. 2 Energetics of the static (a)-(b) and dynamic (c)-(d) approaches for the activation of an NO molecule in its doublet and quartet spin states. Panels (a)-(b) show the evolution of the difference of the total ($\Delta E_{DFT+disp}$), DFT (ΔE_{DFT}), and long-range dispersion (Δ_{disp}) energies with respect to their values at 4.69 Å as a function of the constrained distance between the O and Fe(II). Panels (c)-(d) show the evolution of the mean force of constraint, which is integrated to compute free energies (ΔG) in AIMD simulations as a function of Fe(II)-O constrained distance.

3.2 Nitrogen dioxide

The NO_2 molecule, similar to NO, is a free radical with one unpaired electron. Here we consider two spin states, the doublet (ground state) and the quartet. Our calculations carried out with both the static and dynamic approaches indicate that the Fe(II) oxidation is thermodynamically favourable at 298 K. Mechanistically, the calculations indicate that the overall oxidation involves two steps. The initial step is the abstraction of an O atom from NO_2,

$$\mathrm{Fe(II)} + \mathrm{NO_2} \longrightarrow \mathrm{Fe(III)O{—}NO}, \quad (4)$$

which is followed by the detachment of the resulting NO molecule from the Fe(III)O(oxo)-NO intermediate,

$$\mathrm{Fe(III)O{—}NO} \longrightarrow \mathrm{Fe(IV)O} + \mathrm{NO}. \quad (5)$$

This mechanism is consistent with the evolution of the Mulliken charges and spin charges during the formation of the Fe-O bond. In particular, from the data plotted in Fig. S4 for the doublet, the Mulliken net charge is 1.07 with a spin on Fe at the end of the process is 4.28, indicating that there are 4 unpaired electrons on this atom, consistent with an incipient quintet Fe(IV)O moiety.

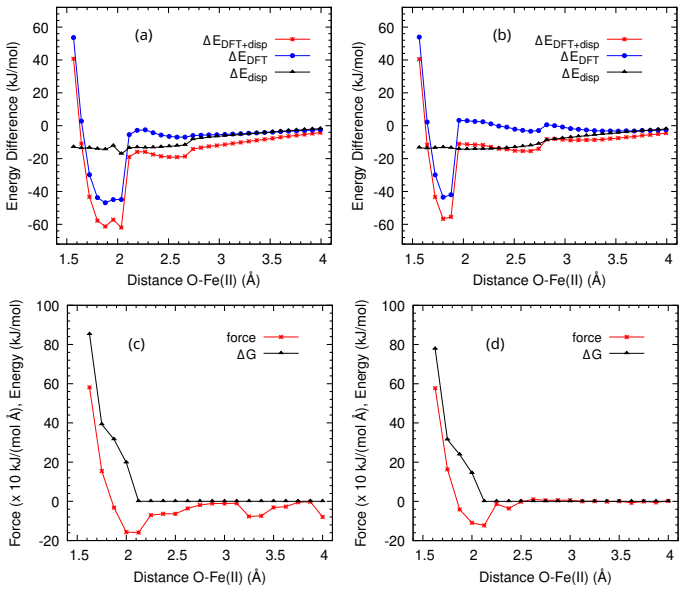

Fig. 3 Energetics of the static ((a) for doublet and (c) for quartet) and dynamic ((b) for doublet and (d) for quartet) approaches for the activation of an NO_2 molecule in its singlet spin configuration at a Fe(II) site.

Reactions 4 for the NO_2 abstraction and 5 for the subsequent NO departure are thermodynamically favourable according to the enthalpies calculated using the static method. As shown in Figure 3(a), the system is more stable once the complex Fe(III)O—NO in MOF-74 is formed than in its previous configuration with the doublet NO_2 far away from the Fe(II) site. Here, we observe that as the O atom of NO_2 begins to form the bond with Fe(II) at a distance of 1.80 Å, the atoms close to Fe in the MOF structure and the NO_2 molecule rearrange to promote the formation of the Fe-O bond. This structural rearrangement is responsible for the drop in the system's total energy observed at around 2.0 Å. Hence, the process is exothermic, with an enthalpy $\Delta H^{S=2}_{NO_2,ads}$ of 49.69 kJ/mol at 2.04 Å for doublet NO_2 taking place according to

$$\mathrm{Fe(II)} + \mathrm{NO_2} \longrightarrow \mathrm{Fe(II)O{—}N\text{-}O}. \quad (6)$$

NO_2 in its quartet state exhibits a similar behaviour, as shown in Figure 3(c), where a similar decrease in total energy occurs at a slightly shorter distance of 1.65 Å. This distance is consistent with the predictions and measurements reported in the literature for

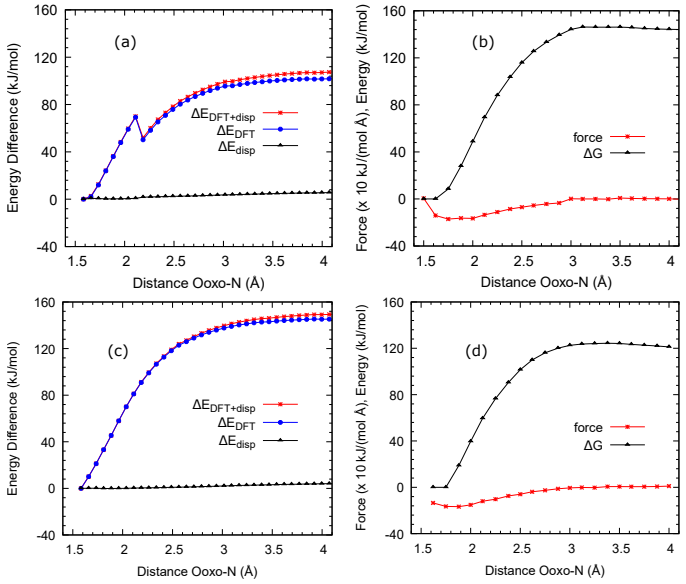

Fig. 4 Energetics of the static (a for doublet and c for quartet) and dynamic (b for doublet and d for quartet) approaches for the detachment of NO from the Fe(IV)O centre upon the uptake of NO_2 in its singlet spin configuration by the Fe(II) active site.

the length of the Fe(IV)O bond. Previously, predictions of 1.59-1.63 Å were reported using other DFT levels of theory, such as LDA,[86] BLYP,[72,73] and B3LYP[72–74] in MOF-74,[50] and in different environments such as gas-phase complexes with values between 1.60 and 1.62 Å,[64] and around 1.65 Å for many complexes measured experimentally (see Table I in Ref. 87). The enthalpy of reaction $\Delta H^{S=4}_{NO_2,ads}$ is 45.72 kJ/mol, which is similar to that predicted for the doublet configuration. As in the case of NO, the role of van der Waals is significant for both spins, with differences up to 14.45 kJ/mol.

The formation of a Fe-O bond is confirmed by the results of the AIMD calculations, shown in Figures 3(b) and (d). The mean force of the constraint for the Fe-O distance is virtually zero at large separations and negative for separations shorter than 2.5 Å, indicating an attractive (bonding) interaction, and reaches a minimum at 2.12 Å of -159.33 kJ/(mol Å) for the doublet and of -122.70 kJ/(mol Å) for the quartet. After this point, the force starts to increase in both cases, reaching a value of 581.44 kJ/(mol Å) for the doublet and 577.34 kJ/(mol Å) for the quartet at 1.63 Å. The free energy of reaction for the formation of Fe-O bond is obtained by integrating the mean force between 2.12 Å and 1.63 Å, which yields values of $\Delta G^{S=2}_{NO_2,ads}$ = 85.28 kJ/mol and $\Delta G^{S=4}_{NO_2,ads}$ = 77.83 kJ/mol. From these values we estimate the reaction entropies $\Delta S^{S=2}_{NO_2,ads}$ = -118.64 J/(mol K) and $\Delta S^{S=4}_{NO_2,ads}$ = -107.03 J/(mol K) for the two spin states.

The decrease in free energy as the NO_2 molecule approaches the Fe(II) site indicates that the reaction of this molecule with Fe(II) is favourable at zero as well as at room temperature and that the process requires no activation step. In an actual reaction, in which a reactive gas or fluid (rather and isolated NO_2 molecule) diffuses in the MOF pores, the reaction can therefore be diffusion controlled, with reaction barriers expected to be of the order of 5-10 kJ/mol.[88] Our results also indicate that, at room temperature, the entropic contribution to the reactive event can be very large regardless of the spin state, suggesting that two factors, i.e. all the vibrations within the MOF structure and the atomic disorder of the incoming molecule, that are naturally accounted for in molecular dynamics trajectories have a significant role in the uptake of NO_2 by Fe(II). Thus, our results imply that reaction barriers remarkably vary when imposing a finite temperature.

Once the bonding of Fe and O has taken place, the formation of a free reactive Fe(IV)O moiety occurs *via* the detachment of an NO molecule,

$$\text{Fe(III)O—N-O} \longrightarrow \text{Fe(IV)O} + \text{NO}. \qquad (7)$$

As shown in Figure 3(c), according to our static calculations the detachment of NO requires an enthalpy $\Delta H^{S=2}_{NO_2,dep}$ = 108.80 kJ/mol for the doublet and $\Delta H^{S=4}_{NO_2,dep}$ = 149.71 kJ/mol for the quartet. In the case of the doublet, we observe a discontinuity at 2.2 Å caused by a geometric rearrangement of the NO when this molecule is moving away from the Fe(IV)O site (see Figure S7). By contrast, the AIMD simulations indicate that the departure of the NO molecule requires free energies at room temperature that are more similar to each other than the corresponding enthalpies, $\Delta G^{S=2}_{NO_2,dep}$ = 144.08 kJ/mol for the doublet and $\Delta G^{S=4}_{NO_2,dep}$ = 121.20 kJ/mol for the quartet. As a consequence, the estimated entropies of detachment are very different in the two spin states: $\Delta S^{S=2}_{NO_2,dep}$ = -117.60 J/(mol K) and $\Delta S^{S=4}_{NO_2,dep}$ = 95.03 J/(mol K).

These results show the relevance of entropic effects, along with the spin state, in the NO_2 reactivity after the Fe(II) oxidation and the Fe(IV)-O bond formation process. At room temperature, they are responsible for bringing the free energy of NO detachment for the two spin states much closer to each other than the corresponding enthalpies. Hence, they can influence the preference for the formation of a free reactive Fe(IV)O species to occur with a single-state or multi-state (spin) reactivity. According to our predictions, a crossover between these two regimes could be observed as a function of the reaction temperature. We also notice that the reaction entropies for the NO detachment step are relatively large and of opposite sign. The negative entropy contribution is responsible for the lower free energy barrier in the quartet state compared to the doublet for this process. Thus, this negative entropy makes more favourable the detachment step in the quartet state. According to our calculations, the difference in energy between the quartet and doublet state ($\Delta E^{diffS}_{total} = E^{S=4}_{total} - E^{S=2}_{total}$) amounts to 37.30 kJ/mol before the NO_2 molecule starts to interact with Fe(II). However, after the abstraction step, when NO is still in the vicinity of the metal centre at an O(oxo)-N separation of 1.58 Å, the quartet state becomes more stable (ΔE^{diffS}_{total} = -24.11 kJ/mol). We argue that this transition to the quartet state can favour the detachment step through off-site exchange repulsion interaction. After the detachment, ΔE^{diffS}_{total} increases, reaching a value of -12.84 kJ/mol at 2.11 Å, corresponding to the Ooxo-N distance at which the rearrangement of the doublet NO molecule is observed. At higher distances, the doublet returns

to be the ground spin-state of the NO molecule. For instance, at 2.19 Å, ΔE_{total}^{diffS} amounts to 15.20 kJ/mol.

In turn, the variations of the reaction entropy result from those experienced by the enthalpy and free energy by enforcing different spin states. Indeed, it has been claimed that low and high spin states can vary the reaction enthalpy and energetics of organometallic ligands by several tens of kJ/mol in two-state reactivity conditions.[89,90] Further entropic effects predicted in our study include the number of reaction steps in the overall Fe(II)-to-Fe(IV)O conversion. For instance, although when this process is carried out using NO_2 the reaction mechanism remains a two-step process (oxidation plus detachment), we will show later that in the case of N_2O, entropic effects can drive the reaction to occur *via* a concerted single-step mechanism, in which a reduced species is simultaneously released during the oxidation of Fe(II).

3.3 Nitrous oxide

For nitrous oxide our static and dynamic methods predict an initial O abstraction,

$$\mathrm{Fe(II)} + \mathrm{N_2O} \longrightarrow \mathrm{Fe(III)O{—}N\text{-}N}, \tag{8}$$

to form the complex Fe(III)O—N-N, followed by the detachment of an N_2 molecule

$$\mathrm{Fe(III)O{—}N\text{-}N} \longrightarrow \mathrm{Fe(IV)O} + \mathrm{N_2}. \tag{9}$$

At variance with the reactions studied above, we find that in this case that the detachment reaction 9 takes place during the activation step 8. This concurrence indicates that the N_2 molecule is produced and departs concertedly with the formation of the Fe-O bond in the Fe(IV)O. Therefore, we can only consider the energetics of O abstraction illustrated in Figure 5, from which we estimate an abstraction enthalpy barrier $\Delta H_{N_2O,ads}$ of 184.19 kJ/mol at a Fe-O separation of 1.57 Å. In contrast, the AIMD simulations suggest that the transition state for the Fe-O bond formation takes place at a separation of 1.82 Å, where the mean force of the Fe-O distance constraint, 5.40 kJ/(mol Å), is sufficiently close to assume that the Fe-O bond has been established. We estimate a free energy barrier $\Delta G_{N_2O,ads}$ of 28.64 kJ/mol for the abstraction of O from N_2O and the simultaneous detachment of N_2 from the integration of the mean force up 1.82 Å. From this value and the calculated enthalpy of reaction, we estimate a large entropic contribution $\Delta S_{N_2O,ads}$ = 518.50 J/(mol K) for the overall reaction, which is much larger than those found for nitrogen-based oxidants in this work.

The large increase in entropy upon formation of free Fe(IV)O is likely to be caused by the increase in vibrational freedom caused by the formation of N_2. A positive entropy has been observed also in the case of NO_2 in its quartet state ($\Delta S_{NO_2,dep}^{S=4}$ = 95.03 J/(mol K)), and it has been shown to contribute to favouring the detachment of NO after the Fe(II) oxidation step. In the case of N_2O, the entropic contribution is sufficiently large in absolute value to induce a transition from a step-wise to a concerted mechanism of oxidation plus detachment.

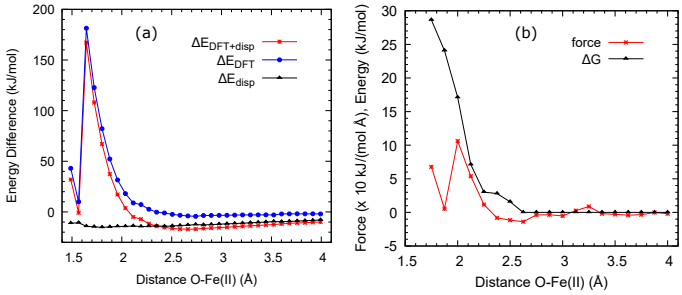

Fig. 5 Energetics of the static (a) and dynamic (b) approaches for the activation of a N_2O molecule by the Fe(II) active site.

3.4 Dinitrous dioxide

In the case of dinitrous dioxide (N_2O_2 or O=N-N=O), the static and dynamic simulation approach predict different outcomes. On one hand, the data in Figure 6, obtained with the static method, shows the presence of two maxima in the total energy, one at a Fe(II)-O distance of 1.88 Å and one at 1.57 Å. The first peak at 1.88 Å is the consequence of a geometric rearrangement of the N_2O_2 molecule, which experiences large long-range interactions with the MOF structure in the vicinity of the Fe(II) ion. The second maximum is associated with the reaction

$$\mathrm{Fe(II)} + \mathrm{O{=}N\text{-}N{=}O} \longrightarrow \mathrm{Fe(IV)O} + \mathrm{N\text{-}N{=}O}, \tag{10}$$

which leads to the formation of the Fe(IV)O moiety. Similar to the case of N_2O, the oxidation of Fe(II) to Fe(IV)O and the detachment of the reduced N_2O molecule occur through a concerted mechanism. The overall enthalpy for the production of Fe(IV)O is $\Delta H_{N_2O_2,ads}$ = 95.41 kJ/mol, with a significant contribution from van der Waals dispersion of up to 20.37 kJ/mol. For this case, the calculation of the corresponding free energy using AIMD could not be carried out at room temperature, as the N_2O_2 molecules decomposes into its constituent NO monomers. This finding is consistent with the weak nature of the N-N interactions responsible for the stability of the N_2O_2 molecule. Based on these findings for N_2O in the previous section, we hypothesise that, since this reaction for N_2O_2 is predicted to have a single step at 0 K, the entropic contributions at high temperature are expected to be large and positive, bringing be a gain of vibrational freedom on the system. Most likely, this increase is because the bond between the two NOs in the N_2O_2 dimer splits at finite temperature.

3.5 Oxygen

Turning now our attention to nitrogen-free molecules, we continue our analysis with O_2 in its singlet (S = 1) and triplet (S = 3) states. While O_2 is a triplet in its ground state, singlet O_2 has been shown to play an important role in the formation of Fe(IV)O moieties in dinuclear Fe(II) complexes.[91,92] According to our calculations, the activation of O_2 in the presence of Fe(II) may or may not happen depending on the reaction temperature. We model the initial uptake of one O atom assuming that the reaction has of the form

$$\mathrm{Fe(II)} + \mathrm{O{=}O} \longrightarrow \mathrm{Fe(III)O{–}O} \tag{11}$$

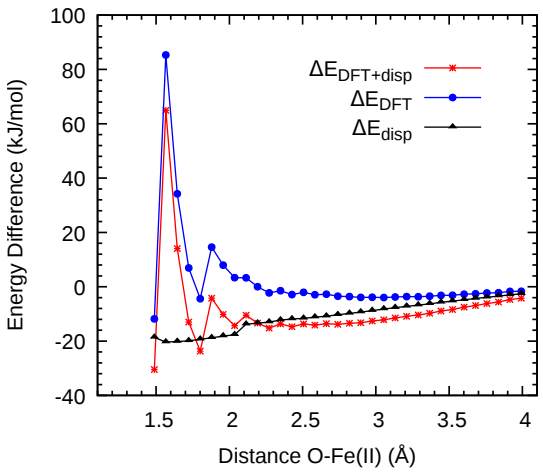

Fig. 6 The difference of the total ($\Delta E_{DFT+disp}$), DFT (ΔE_{EDFT}), and long-range dispersion (Δ_{disp}) energies with respect to their values at 4.00 Å *vs.* the distance between the O and Fe(II) depleted site during the N_2O_2 abstraction step.

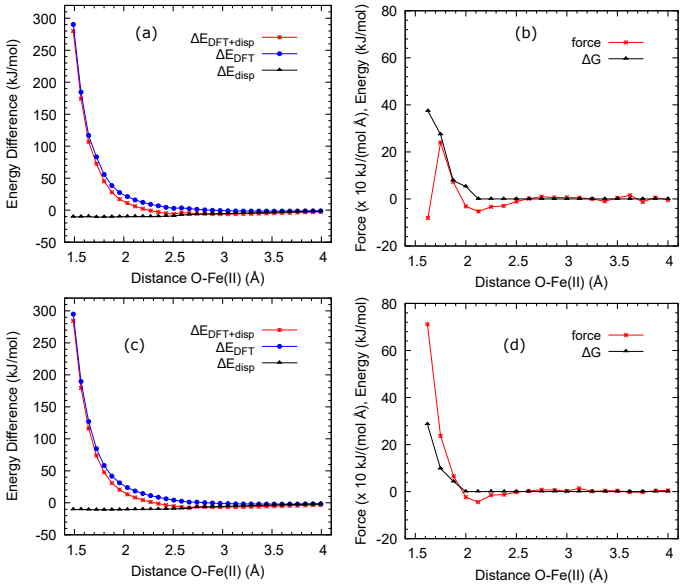

Fig. 7 Energetics of the static ((a) for singlet and (c) for triplet) and dynamic ((b) for singlet and (d) for triplet) approaches for the activation of a O_2 molecule in its singlet spin configuration by the Fe(II) active site.

or

$$\mathrm{Fe(II)} + \mathrm{O{=}O} \longrightarrow \mathrm{Fe(IV)O} + \mathrm{O{:}}. \qquad (12)$$

Our static calculations predict that the contact of singlet and triplet O_2 with Fe(II) develops according to reaction 11, with the second oxygen atom bonded to the newly-formed Fe(III)O group. Imposing a shorter distance between the Fe(II) and the O_2's oxygen only increases the system's total energy, as shown in Figures 7(a) and (c), where no maxima are visible for distances between 1.6 and 1.8 Å. This behaviour indicates that the uptake of oxygen is energetically unfavourable at 0 K. By contrast, when thermal vibrations are allowed in the AIMD simulations at room temperature, the mean force between Fe(II) and an incoming singlet O_2 molecule is attractive when the Fe-O separation is shorter than ca. 1.5 Å (Figure 7(b)). The mean force increases rapidly as the Fe-O distance is shortened, with a maximum point of 240.32 kJ/(mol Å) at 1.75 Å before reaching a negative value of -80.68 kJ/(mol Å) at 1.62 Å. The integration of the force from its minimum at 2.13 Å yields a free energy $\Delta G^{S=1}_{O_2,ads} = 37.42$ kJ/mol. However, the mean force for the triplet state exhibits a large increase as the Fe-O distance is shortened. Indeed, this mean force is never negative, hence the reaction is not occurring in this spin state. This finding is consistent with the low reactivity of the triplet state, which needs to be "activated" (*i.e.* converted to a singlet) to carry out the electron transfer from Fe(II). Therefore, we cannot formally define a free energy of reaction for the triplet state and thus, its associated entropy. On the contrary, for the singlet state this property is well-defined with a value of $\Delta S^{S=1}_{O_2,ads} = 252.10$ J/(mol K), indicating that this process is subject to very strong entropic effects.

An important difference between the static calculations and the finite-temperature AIMD simulations is that, in the latter case, we observe the departure of the radical O after the oxidation of Fe(II) to Fe(IV).

3.6 Ozone

In the case of ozone, we propose an O-abstraction mechanism similar to the one of oxygen, *i.e.*

$$\mathrm{Fe(II)} + \mathrm{O{=}O\text{-}O} \longrightarrow \mathrm{Fe(III)O{-}O{=}O}, \qquad (13)$$

which needs further steps of rebound and/or departure, or

$$\mathrm{Fe(III)O{-}O{=}O} \longrightarrow \mathrm{Fe(IV)O} + \mathrm{O{=}O}. \qquad (14)$$

Other possible mechanisms can include the reaction of the Fe(III)O-O=O with another O_3 molecule to possibly yield two O_2 molecules. However, our static and dynamic calculations reveal that reaction 13 is thermodynamically favourable and leads to the release of an O_2 molecule from the Fe(IV)O site. Figure 8(a) shows the unusual energy profile obtained from our static calculations, which exhibits a significant decrease of the system's total energy from 3.06 to 1.89 Å. In comparison with oxygen, this profile suggests that ozone tends to get closer to Fe(II) than to remain far away from it. We believe that a potential cause for such preference may originate from Coulombic effects, with Fe(II) inducing a dipole moment on O_3. This is consistent with the large polarizability of this species (3.08 Å^3 [93]) compared to oxygen (1.56 Å^3 [94]). Furthermore, the O_3 energy profile exhibits a significant decrease starting from -8.44 kJ/mol, at which point one of the O atoms of O_3 is 3.06 Å away from the Fe(II) ion down to -177.29 kJ/mol at 1.89 Å, a point at which the energy very modestly increases to -175.01 kJ/mol at 1.81 Å, yielding a small enthalpy barrier of 2.28 kJ/mol, which coincides with a slight geometric readjustment of the Fe(II) nearest neighbours to better accommodate the incoming ozone's oxygen. As the O_3 oxygen is displaced closer to the Fe(II) site, the molecule progressively decomposes, and an O_2 molecule evolves which moves towards the centre of the MOF cavity. The concurrent departure and Fe-O bond forma-

tion are reflected energetically as a decrease of the system's total energy down to its global minimum of -207.21 kJ/mol at 1.66 Å, with a local maximum at 1.97 Å due to atomic rearrangements of the unconstrained atoms in the system. The distance of 1.66 Å is similar to that observed for O_2, and provides an estimate of the equilibrium bond length of the Fe(IV)O group.

Data for this reaction collected from the AIMD simulations is shown in Figure 8(b). The mean force of the Fe-O(O_3) distance constraint exhibits an average close to zero up to 3.0 Å, at which point it starts to increase to then exhibit a minimum of -198.474 kJ/(mol Å) at 2.13 Å. It then increases to a maximum of 185.62 kJ/(mol Å) at 1.75 Å and finally decreases to -54.60 kJ/(mol Å) at 1.62 Å. An integration of the mean force starting at 2.13 Å, where the Fe-O is likely to begin forming, yields a free energy $\Delta G^{S=1}_{O_3,ads} = 49.24$ kJ/mol. This energy differs substantially from the enthalpy estimate, and the entropy for this process $\Delta S_{O_3,ads}$ has a large negative value of -156.53 J/(mol K). According to the finding of the previous subsections, this entropy should be positive as the overall oxidation of Fe(II) is carried out in one step; however, some factors might explain this unexpected result for O_3. For instance, we obtain a very small enthalpy barrier, which may be caused by the significant role of the molecular polarizability during the reaction. The free energy barrier is thus here much larger than for the reactions carried out in the presence of NO_2 or N_2O (see Table 1).

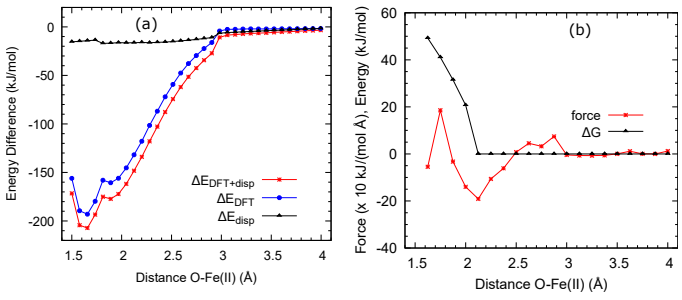

Fig. 8 Energetics of the static (a) and dynamic (b) approaches for the activation of a O_3 molecule by the Fe(II) active site.

3.7 Hydrogen peroxide

For H_2O_2 we consider the following mechanism for the oxidation of Fe(II):

$$\text{Fe(II)} + \text{H}_2\text{O}_2 \longrightarrow \text{Fe(IV)O} + \text{H}_2\text{O}. \qquad (15)$$

This reaction leads to the formation of a water molecule along with an Fe(IV)O group. For the O-abstraction reaction from H_2O_2 the static and dynamic models both indicate that the Fe(II) ion initially binds an OH group,

$$\text{Fe(II)} + \text{H-O-O-H} \longrightarrow \text{Fe(III)-O-H} + \text{O-H}\cdot, \qquad (16)$$

to produce the intermediate complex Fe(III)-O-H along with an O-H· radical. Figure 9(a) shows that this abstraction is thermodynamically favourable at 0 K with a well-defined enthalpy barrier $\Delta H_{H_2O_2,abs} = 68.88$ kJ/mol from the energy minimum at 2.11 Å to the maximum at 1.64 Å. Dispersive van der Waals forces play a remarkable role in this process, reaching values as large as -17.71 kJ/mol at 1.64 Å. This finding indicates not only that the H_2O_2 molecule experiences a large attractive force at distances for which the Fe(II)-O bond begins to form, but also that the attraction exists for much larger separations. We therefore conclude that the reduction of H_2O_2 at the Fe(II) centre at 0 K is largely driven by long-range interactions.

At room temperature, however, the AIMD simulations show that the long-range interactions have only a weak influence on the overall mean force between Fe(II) and O. As shown in Figure 9(b), negative (attractive) mean forces occur only for Fe-O separations as short as 2.0 Å, indicating no repulsion between the Fe(II) and the H_2O_2 molecule exists before reaching this separation. Only a slightly higher repulsion is also observed in the case of O_2, which suggests that the higher polarizability of the hydrogen peroxide (2.12 Å^3) [95] make the charge-dipole interactions between Fe(II) and H_2O_2 dominant over the dispersive interactions, and the contribution of the former *shadows* that of the latter. We estimate a free energy barrier $\Delta G_{H_2O_2,abs} = 41.34$ kJ/mol, from the integration of the mean force between 1.88 and 1.62 Å, along with a positive entropy $\Delta S_{H_2O_2,abs} = 91.80$ J/(mol K), which can be a consequence again that the vibrational freedom increases as the HO-OH bond is split to form Fe(IV)O and an OH radical.

We then study the rebound of the OH· radical to the Fe(III)O–O-H which leads to the formation of Fe(IV)O and H_2O,

$$\text{Fe(III)-O-H} + \text{O-H}\cdot \longrightarrow \text{Fe(IV)Ooxo} + \text{H-O-H}. \qquad (17)$$

Figure 9(c) shows that the static method predicts that the rebound of OH· has a well-defined enthalpy barrier $\Delta H_{H_2O_2,reb} = 73.13$ kJ/mol, with a total energy maximum of 63.18 kJ/mol at 1.19 Å and a minimum of -9.950 kJ/mol at 2.28 Å. At these distances, a water molecule is formed, which moves away from the Fe(IV)O site to a distance of 2.28 Å. Furthermore, we model the detachment of the water molecule to longer distances from this site with static calculations. Figure 9(e) shows that this process requires an enthalpy $\Delta H_{H_2O_2,dep} = -25.63$ kJ/mol. This negative value indicates that this process is thermodynamic favourable, releasing energy as the water molecule moves away from the Fe(IV)O group. In contrast, in the AIMD simulations at room temperature, the rebound step and the water molecule departure are concerted. Therefore, we assume that the free-energy barrier for the rebound $\Delta G_{H_2O_2,reb}$ also includes a contribution from the H_2O detachment, $\Delta G_{H_2O_2,dep}$. From the mean force shown in Figure 9(d), we calculate a free energy for the rebound step $\Delta G_{H_2O_2,reb} = 67.94$ kJ/mol at 1.00 Å. We also estimate entropies of 91.80 J/(mol K) for the abstraction, 17.30 J/(mol K) for the departure, and -85.43 J/(mol K) for the detachment assuming $\Delta G_{H_2O_2,dep} = 0.0$ kJ/mol.

If we compare our results with those available from the literature on the generation of Fe(IV)Ooxo, we find significant differences. For instance, the production of Fe(IV)O with hydrogen peroxide in iron complexes in pyridine-azamacrocycles reported an overall enthalpy of 53 kJ/mol, entropy of -25 J/(mol K), and free energy of 60 kJ/mol. In another experimental work, the activation of non-heme Fe(II) with H_2O_2 [96] required an enthalpy of 16.32 kJ/mol and a high entropy of -156.06 J/(mol

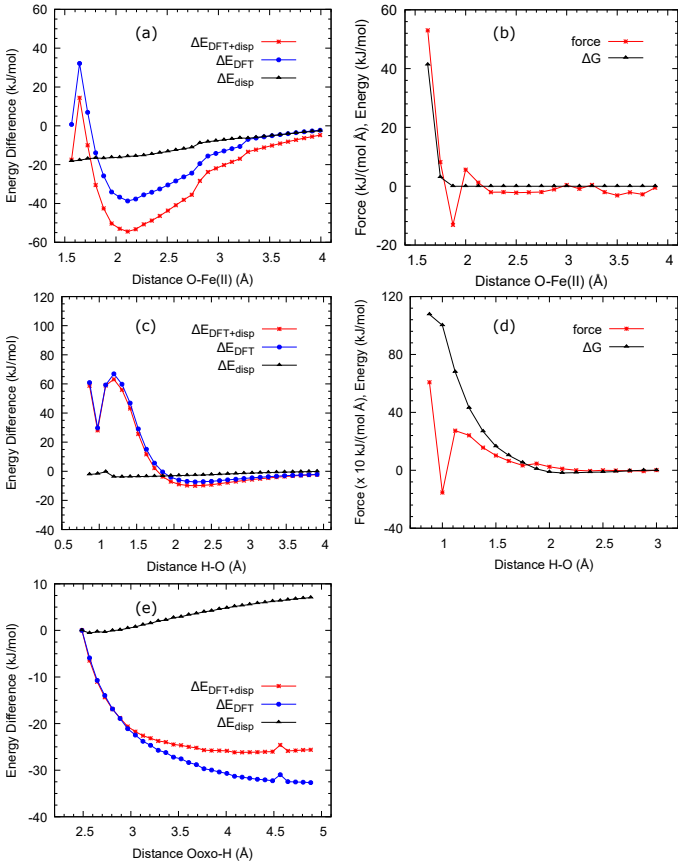

Fig. 9 Energetics of the abstraction (a and b), rebound (c and d), and detachment (e) involved in the oxidation of Fe(II) with H_2O_2. The left-hand side panels show profiles obtained using the static for the difference of the total ($\Delta E_{DFT+disp}$), DFT (ΔE_{EDFT}), and long-range dispersion (Δ_{disp}) components of the enthalpy with respect to their values at 4.00 Å as a function of the distance between O and Fe(II). The right-hand side panels show the evolution of the mean force of constrain for the Fe(II)-O distance and the corresponding integrated free energies (ΔG) obtained from the AIMD simulations.

K).[97] These values are notably dissimilar from our predictions of 116.38 kJ/mol for enthalpy, 23.67 J/(mol K) for entropy, and 109.28 kJ/mol for free energy. These discrepancies might arise from differences in the local environment hosting the Fe(II) ion or from chemical factors, such as the role of pH or the reactant's concentration. Nonetheless, they evidence the relevance of entropic effects in the generation of Fe(IV)O from Fe(II), and hence, the need to predict them with calculations, which can provide a dual representation of enthalpy and free energy.

Based on the calculated free energies, we conclude that, in the case of H_2O_2, similarly to N_2O and O_2, the entropy contribution reduces the free energy barriers for the abstraction and rebound steps. However, the detachment step deserves a special analysis given that the unlike with NO_2, the total energy of the system decreases as the resulting water molecule moves away from the Fe(IV)Ooxo site. By comparing each one of the energy contributions output by CP2k between in the departure steps for the quartet NO_2 (Figure 4(d)) and H_2O_2 (9 (e)), we find that for the latter our static calculations predicts the total energy reduction is caused by the much stronger decrease of the core Hamiltonian, i.e. nuclear plus electronic kinetic contributions, which cannot be compensated by lower weakening of the Hartree potential, exchange-correlation, Hartree-Fock exchange, and dispersion energies. Therefore, the nuclear-nuclear interactions and the kinetic energy of the electrons in the vicinity of the water molecule are significantly affected as this molecule moves away from the Fe(IV)O site. Based on this analysis, we infer that the negative enthalpy for the detachment suggests that the system tends to be more stable when this molecule leaves the Fe(IV)O site at 0 K, which is consistent with the observed simultaneous occurrence of the detachment and rebound steps observed at finite temperature in the AIMD simulations.

In summary, according to the results presented above, the generation of Fe(IV)O requires a three-step mechanism (O-abstraction, rebound and detachment) only in the case of NO_2 and H_2O_2. This is shown in Figure 10, where we plot the reaction enthalpy, free energy, and entropy associated to the initial abstraction, rebound, and detachment. This figure shows that entropic effects are significant for both molecules due to the large difference between their enthalpy and free energy of reaction. This discrepancy is also found for the other oxidants.

In Table 1 we list the overall enthalpy, free energy, and entropy as the summation for all reaction steps, even though for NO, N_2O, N_2O_2, O_2, and O_3 only the abstraction is enough to generate Fe(IV)O. Striking differences are observed between the static and dynamic models of the reactions. On one hand, N_2O, O_2 and O_3 exhibit lower free energy barriers for the Fe(II)-to-Fe(IV)O oxidation at 300 K compared to NO_2 and H_2O_2. However, O_3 and H_2O_2, followed by NO_2, have the lowest enthalpy, which indicates the importance of entropic effects in the reactions. These are particularly relevant for N_2O, O_2, and O_3. A proper description of the oxidation of Fe(II) to Fe(IV)O in a MOF environment needs therefore to account explicitly for entropic contributions. Also, as we have shown, properties of the oxidant such as spin state and polarizability can play a central role in influencing which reaction steps take place and which one of these is the rate limiting one.

Finally, the data listed in Table 1 indicate the existence of a link between oxidant reactivity in the gas phase and lower abstraction enthalpy barriers for the solid-state reactions. For the rebound and detachment steps involving the most reactive species (NO_2, O_3 and H_2O_2), entropies are usually negatives. O_2 and N_2O exhibit the largest entropies and enthalpies of reaction in the solid state, with quartet NO_2. One surprising finding is that, among all the oxidants examined in this study, singlet O_2, which is by far the most reactive species in the gas phase, is not highly reactive in the solid state in the exclusive presence of mononuclear Fe(II) centres. Experimentally, the picture could be quite different, because of the potential existence of di- or polynuclear Fe(II) sites and the concurrent reaction of more than one O_2 molecule reacting at a given time. Similar considerations likely hold also for NO.

4 Conclusions

We have modelled the oxidation of mononuclear Fe(II) centres supported by MOF-74 to Fe(IV)O in the presence of a number of common oxidant molecules (NO, NO_2, N_2O, N_2O_2, O_2, O_3 and

Molecule (spin state)	Process	ΔH (kJ/mol)	ΔG (kJ/mol)	ΔS (J/(mol K))
NO_2 (doublet)	Abstraction	49.69	85.28	-118.63
NO_2 (quartet)	Abstraction	45.72	77.83	-107.03
NO_2 (doublet)	Detachment	108.80	144.08	-117.60
NO_2 (quartet)	Detachment	149.71	121.20	95.03
N_2O (singlet)	Abstraction	184.19	28.64	518.50
N_2O_2 (singlet)	Abstraction	95.41	–	–
O_2 (singlet)	Abstraction	113.05	37.42	252.10
O_3 (singlet)	Abstraction	2.28	49.24	-156.53
H_2O_2 (singlet)	Abstraction	68.88	41.34	91.80
H_2O_2 (singlet)	Rebound	73.13	67.94	17.30
H_2O_2 (singlet)	Detachment	(-25.63)	(0.00)	(-85.43)

Table 1 List of calculated reaction enthalpies ΔH, free energies ΔG, and entropies ΔS for the possible reaction steps (abstraction, rebound and detachment) of the conversion Fe(II) to Fe(IV)Oxo. The detachment step for H_2O_2 is barrier-less and the enthalpy value listed corresponds to the energy difference before and after the migration of the product H_2O molecule away from the Fe(IV)O group. The entropy change is computed in this case, assuming that the free energy for detachment is zero. See main text for further details.

H_2O_2) using periodic DFT calculations. We have used two methods, a static approach, in which the oxidation of Fe(II) is simulated through a series of structural optimizations at 0 K, yielding enthalpy barriers of reaction, and the dynamic approach, which estimates free energies of reaction at room temperature (300 K). A comparison of the two methods highlights important mechanistic differences occurring depending on the temperature at which the interaction of the oxidant with Fe(II) occurs, on the spin state of the oxidant and, possibly, on its molecular polarizability. In all cases, finite-temperature entropic effects are shown to play important roles in promoting or disfavouring the oxidation of Fe(II). N_2O (in its singlet ground state), O_2 (in the excited singlet state) and H_2O_2 exhibit large positive entropic contributions, which substantially reduce the reaction barrier at room temperature compared to 0 K. The opposite is observed in the case of NO_2 (doublet and quartet) and O_3. In these cases, large *negative* entropies are responsible for increasing reaction barriers at room temperature at various stages of the reaction. For O_3, a more than twenty-fold increase in the reaction barrier is observed at room temperature compared to 0 K. The free energy barrier for the oxidation of Fe(IV)O and the evolution of O_2 remains yet sufficiently low to make this reaction favourable even at room temperature.

Based on these outcomes, our work highlights the importance of entropic effects in the oxidation of MOF-supported Fe(II) centres to Fe(IV)O. These results indicate that oxidants capable of generating Fe(IV)O species in abiotic conditions, such as H_2O_2 and O_3, along with O_2 and N_2O, offer the potential to act as suitable agents for the generation of reactive ferryl ions in an MOF environment and in their regeneration in Fe(IV)O-catalyzed reactions, in which Fe(IV)O is reduced back to Fe(II). In addition, our calculations predict that the efficiency of these processes typically exhibits a strong dependence of the reaction temperature. The mechanistic details of the chemical processes and the sign and magnitude of the entropic contribution to the reaction free energies determine whether the conversion of Fe(II) to Fe(IV)O may occur more easily at higher or lower temperatures.

Conflicts of interest

There are no conflicts to declare.

Acknowledgements

This research was supported in part by the University of Pittsburgh Center for Research Computing through the resources provided and by STFC Scientific Computing Department's SCARF cluster.

References

1 F. Saiz and L. Bernasconi, *Catal. Sci. Technol.*, 2022, **12**, 3069–3087.
2 C. Wang, B. An and W. Lin, *ACS Catal.*, 2018, **9**, 130–146.
3 M. J. da Silva, *Fuel Process. Tech.*, 2016, **145**, 42–61.
4 Y. Dong, L. J. Que, K. Kauffmann and E. Muenck, *J. Am. Chem. Soc.*, 1995, **117**, 11377–11378.
5 B. Meunier, G. Brudvig, J. L. Mclain, S.-i. Murahashi, V. Pecoraro, D. Riley, A. Robert, J. Rodriguez, R. Sheldon, J. Valentine *et al.*, *BiomimBiomimetic Oxidations Catalyzed by Transition Metal Complexes*, World Scientific, 2000.
6 J. C. Price, E. W. Barr, B. Tirupati, J. M. Bollinger and C. Krebs, *Biochem.*, 2003, **42**, 7497–7508.
7 M. Costas, M. P. Mehn, M. P. Jensen and L. Que, *Chem. Rev.*, 2004, **104**, 939–986.

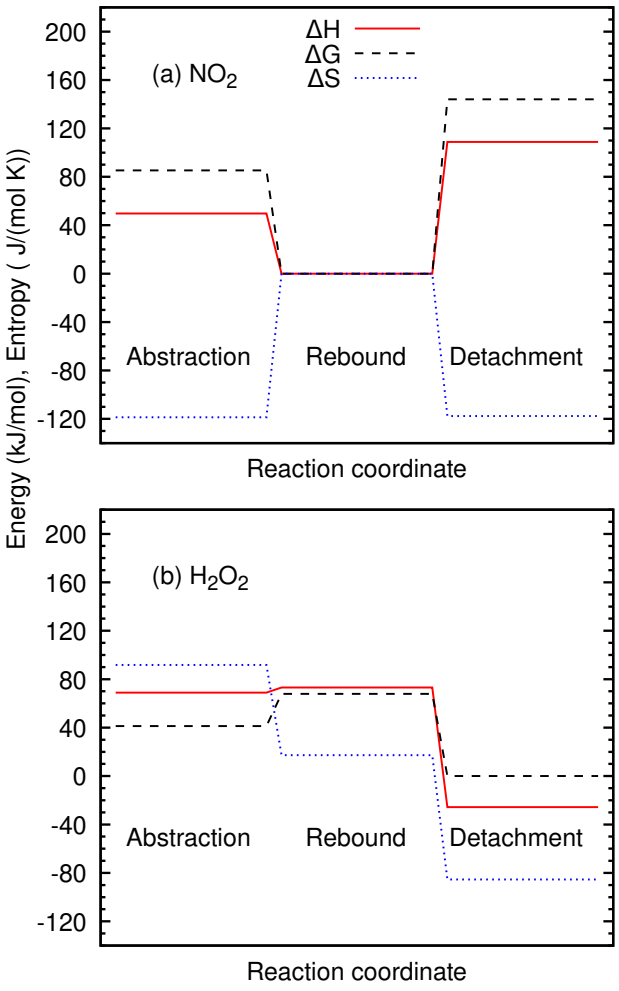

Fig. 10 Calculated enthalpies (ΔH), free energies (ΔG) and entropies (ΔS) for the oxygen abstraction of nitrogen dioxide (a) and hydrogen peroxide (b), and rebound of the radical OH · for the former, and detachment of the nitrogen oxide and water, respectively.

8 B. Meunier, S. P. De Visser and S. Shaik, *Chem. Rev.*, 2004, **104**, 3947–3980.

9 L. Que and W. B. Tolman, *Nature*, 2008, **455**, 333–340.

10 E. D. Bloch, W. L. Queen, R. Krishna, J. M. Zadrozny, C. M. Brown and J. R. Long, *Science*, 2012, **335**, 1606–1610.

11 P. Verma, X. Xu and D. G. Truhlar, *J. Phys. Chem. C*, 2013, **117**, 12648–12660.

12 A. N. Biswas, M. Puri, K. K. Meier, W. N. Oloo, G. T. Rohde, E. L. Bominaar, E. Muenck and L. Que Jr, *J. Am. Chem. Soc.*, 2015, **137**, 2428–2431.

13 P. Verma, K. D. Vogiatzis, N. Planas, J. Borycz, D. J. Xiao, J. R. Long, L. Gagliardi and D. G. Truhlar, *J. Am. Chem. Soc.*, 2015, **137**, 5770–5781.

14 L. Bernasconi, A. Kazaryan, P. Belanzoni and E. J. Baerends, *ACS Catal.*, 2017, **7**, 4018–4025.

15 G. Olivo, O. Cussó, M. Borrell and M. Costas, *JBIC J. Bio. Inorg. Chem.*, 2017, **22**, 425–452.

16 F. Neese and E. I. Solomon, *J. Am. Chem. Soc.*, 1998, **120**, 12829–12848.

17 B. Ensing, F. Buda, P. Blöchl and E. J. Baerends, *Angew. Chem. Int. Ed*, 2001, **40**, 2893–2895.

18 B. Ensing, F. Buda, M. C. Gribnau and E. J. Baerends, *J. Am. Chem. Soc.*, 2004, **126**, 4355–4365.

19 F. Neese, *J. Inorg. Biochem.*, 2006, **100**, 716–726.

20 D. J. Xiao, E. D. Bloch, J. A. Mason, W. L. Queen, M. R. Hudson, N. Planas, J. Borycz, A. L. Dzubak, P. Verma, K. Lee *et al.*, *Nature Chem.*, 2014, **6**, 590.

21 H. Hirao, W. K. H. Ng, A. M. P. Moeljadi and S. Bureekaew, *ACS Catal.*, 2015, **5**, 3287–3291.

22 P. Liao, R. B. Getman and R. Q. Snurr, *ACS Appl. Mat. Int.*, 2017, **9**, 33484–33492.

23 S. Ketrat, T. Maihom, S. Wannakao, M. Probst, S. Nokbin and J. Limtrakul, *Inorg. Chem.*, 2017, **56**, 14005–14012.

24 B. L. Suh and J. Kim, *J. Phys. Chem. C*, 2018, **122**, 23078–23083.

25 M. C. Simons, S. D. Prinslow, M. Babucci, A. S. Hoffman, J. Hong, J. G. Vitillo, S. R. Bare, B. C. Gates, C. C. Lu, L. Gagliardi *et al.*, *J. Am. Chem. Soc.*, 2021, **143**, 12165–12174.

26 D. Deng, X. Chen, L. Yu, X. Wu, Q. Liu, Y. Liu, H. Yang, H. Tian, Y. Hu, P. Du *et al.*, *Science Adv.*, 2015, **1**, e1500462.

27 J. Sittiwong, T. Jaturajamrenchai, P. Wongkampuan, N. Somwatcharajit, S. Impeng, T. Maihom, M. Probst and J. Limtrakul, *Molec. Catal.*, 2021, **516**, 111970.

28 S. Kameoka, T. Nobukawa, S.-i. Tanaka, S.-i. Ito, K. Tomishige and K. Kunimori, *Phys. Chem. Chem. Phys.*, 2003, **5**, 3328–3333.

29 A. Rosa, G. Ricciardi and E. J. Baerends, *Inorg. Chem.*, 2010, **49**, 3866–3880.

30 F. Goltl, C. Michel, P. C. Andrikopoulos, A. M. Love, J. Hafner, I. Hermans and P. Sautet, *ACS Catal.*, 2016, **6**, 8404–8409.

31 F. Göltl, S. Bhandari and M. Mavrikakis, *ACS Catal.*, 2021, **11**, 7719–7734.

32 M. Ren, Q. Shi, L. Mi, W. Liang, M. Yuan, L. Wang, Z. Gao, W. Huang, J. Huang and Z. Zuo, *Mater. Today Sustain.*, 2021, **11**, 100061.

33 S. Hyeon, Y.-C. Kim and J. Kim, *Phys. Chem. Chem. Phys.*, 2017, **19**, 21132–21139.

34 M. Ogura, K. Itabashi, J. Dedecek, T. Onkawa, Y. Shimada, K. Kawakami, K. Onodera, S. Nakamura and T. Okubo, *J. Catal.*, 2014, **315**, 1–5.

35 J. G. Vitillo and L. Gagliardi, *Inorg. Chem.*, 2021, **60**, 11813–11824.

36 B. Coq, M. Mauvezin, G. Delahay, J.-B. Butet and S. Kieger, *Appl. Catal. B: Env.*, 2000, **27**, 193–198.

37 M. Mauvezin, G. Delahay, F. Kisslich, B. Coq and S. Kieger, *Catal. Lett.*, 1999, **62**, 41–44.

38 P. Boroń, M. Rutkowska, B. Gil, B. Marszałek, L. Chmielarz and S. Dzwigaj, *ChemSusChem*, 2019, **12**, 692–705.

39 K. Jíša, J. Nováková, M. Schwarze, A. Vondrová, S. Sklenák and Z. Sobalik, *J. Catal.*, 2009, **262**, 27–34.

40 M. L. Bols, B. E. Snyder, H. M. Rhoda, P. Cnudde, G. Fayad,

R. A. Schoonheydt, V. Van Speybroeck, E. I. Solomon and B. F. Sels, *Nat. Catal.*, 2021, **4**, 332–340.
41 B. Chandra, K. M. Hellan, S. Pattanayak and S. S. Gupta, *Chem. Sci.*, 2020, **11**, 11877–11885.
42 P. Comba, D. Faltermeier and B. Martin, *Zeitschrift für anorganische und allgemeine Chemie*, 2020, **646**, 1839–1845.
43 K. Warm, A. Paskin, U. Kuhlmann, E. Bill, M. Swart, M. Haumann, H. Dau, P. Hildebrandt and K. Ray, *Ang. Chem.*, 2021, **133**, 6826–6830.
44 J. Lin, Q. Sun and W. Sun, *RSC Adv.*, 2021, **11**, 2293–2297.
45 D. Schmidl, N. S. Jonasson, E. Korytiaková, T. Carell and L. J. Daumann, *Ang. Chem. Int. Ed.*, 2021, **60**, 21457–21463.
46 J. Deutscher, P. Gerschel, K. Warm, U. Kuhlmann, S. Mebs, M. Haumann, H. Dau, P. Hildebrandt, U.-P. Apfel and K. Ray, *Chem. Comm.*, 2021, **57**, 2947–2950.
47 R. Kumar, M. Sundararajan and G. Rajaraman, *Chem. Commun.*, 2021, **57**, 13760–13763.
48 P. Kumar, B. Anand, Y. F. Tsang, K.-H. Kim, S. Khullar and B. Wang, *Env. Res.*, 2019, **176**, 108488.
49 H. B. Dunford, *Coord. Chem. Rev.*, 2002, **233**, 311–318.
50 F. Saiz and L. Bernasconi, *Phys. Chem. Chem. Phys.*, 2019, **21**, 4965–4974.
51 F. Saiz and L. Bernasconi, *Phys. Chem. Chem. Phys.*, 2020, **22**, 12821–12830.
52 F. Saiz and L. Bernasconi, *Catal. Sci. Technol.*, 2021, **11**, 4560–4569.
53 J. Barbero, M. Alvarez, M. Bañares, M. Peña and J. Fierro, *Chem. Comm.*, 2002, 1184–1185.
54 K. Tabata, Y. Teng, T. Takemoto, E. Suzuki, M. Banares, M. Pena and J. G. Fierro, *Catal. Rev.*, 2002, **44**, 1–58.
55 D. Y. Osadchii, A. I. Olivos-Suarez, Á. Szécsényi, G. Li, M. A. Nasalevich, I. A. Dugulan, P. S. Crespo, E. J. Hensen, S. L. Veber, M. V. Fedin *et al.*, *ACS Catal.*, 2018, **8**, 5542–5548.
56 A. Szécsényi, G. Li, J. Gascon and E. A. Pidko, *ACS Catal.*, 2018, **8**, 7961–7972.
57 Á. Szécsényi, G. Li, J. Gascon and E. A. Pidko, *Chem. Sci.*, 2018, **9**, 6765–6773.
58 Z. Cai, W. Tao, C. E. Moore, S. Zhang and C. R. Wade, *Angewandte Chemie International Edition*, 2021, **60**, 21221–21225.
59 H. Park, M. M. Bittner, J. S. Baus, S. V. Lindeman and A. T. Fiedler, *Inorg. Chem.*, 2012, **51**, 10279–10289.
60 B. E. Snyder, P. Vanelderen, M. L. Bols, S. D. Hallaert, L. H. Böttger, L. Ungur, K. Pierloot, R. A. Schoonheydt, B. F. Sels and E. I. Solomon, *Nature*, 2016, **536**, 317–321.
61 A. S. Rosen, J. M. Notestein and R. Q. Snurr, *Phys. Chem. Chem. Phys.*, 2022, –.
62 C. R. Groom, I. J. Bruno, M. P. Lightfoot and S. C. Ward, *Acta Crystallogr. Sec. B*, 2016, **72**, 171–179.
63 D. S. BIOVIA, *Materials Studio Suite, v.5.5.2,*, 2017.
64 L. Bernasconi, M. J. Louwerse and E. J. Baerends, *Eur. J. Inorg. Chem.*, 2007, **2007**, 3023–3033.
65 A. Stukowski, *Model. Sim. Mat. Sci. Eng.*, 2009, **18**, 015012.
66 J. Hutter, M. Iannuzzi, F. Schiffmann and J. VandeVondele, *Wiley Interdis. Rev.: Comp. Molec. Sci.*, 2014, **4**, 15–25.
67 J. VandeVondele and M. Sprik, *Phys. Chem. Chem. Phys.*, 2005, **7**, 1363–1367.
68 S. Goedecker, M. Teter and J. Hutter, *Phys. Rev. B*, 1996, **54**, 1703–1710.
69 M. Krack, *Theor. Chem. Acc.*, 2005, **114**, 145–152.
70 J. Heyd, G. E. Scuseria and M. Ernzerhof, *J. Chem. Phys.*, 2003, **118**, 8207–8215.
71 H. Iikura, T. Tsuneda, T. Yanai and K. Hirao, *J. Chem. Phys.*, 2001, **115**, 3540–3544.
72 A. D. Becke, *Phys. Rev. A*, 1988, **38**, 3098–3100.
73 C. Lee, W. Yang and R. G. Parr, *Phys. Rev. B*, 1988, **37**, 785–789.
74 S. H. Vosko, L. Wilk and M. Nusair, *Can. J. Phys.*, 1980, **58**, 1200–1211.
75 S. Grimme, J. Antony, S. Ehrlich and H. Krieg, *J. Chem. Phys.*, 2010, **132**, 154104.
76 E. Carter, G. Ciccotti, J. T. Hynes and R. Kapral, *Chem. Phys. Lett.*, 1989, **156**, 472–477.
77 M. Sprik and G. Ciccotti, *J. Chem. Phys.*, 1998, **109**, 7737–7744.
78 S. Nosé, *J. Chem. Phys.*, 1984, **81**, 511–519.
79 W. G. Hoover, *Phys. Rev. A*, 1985, **31**, 1695.
80 L. Bernasconi and E. J. Baerends, *J. Am. Chem. Soc.*, 2013, **135**, 8857–8867.
81 A. Wanat, T. Schneppensieper, G. Stochel, R. van Eldik, E. Bill and K. Wieghardt, *Inorg. Chem.*, 2002, **41**, 4–10.
82 M. J. Kampschreur, R. Kleerebezem, W. W. de Vet and M. C. van Loosdrecht, *Water Res.*, 2011, **45**, 5945–5952.
83 T. C. Harrop, D. Song and S. J. Lippard, *J. Am. Chem. Soc.*, 2006, **128**, 3528–3529.
84 S. Brdarski and G. Karlström, *J. Phys. Chem. A*, 1998, **102**, 8182–8192.
85 C. I. Viquez Rojas and L. V. Slipchenko, *J. Chem. Theory Comput.*, 2020, **16**, 6408–6417.
86 A. D. Becke, *Phys. Rev. A*, 1988, **38**, 3098.
87 A. R. McDonald and L. Que Jr, *Coord. Chem. Rev.*, 2013, **257**, 414–428.
88 K. N. Houk, N. G. Rondan and J. Mareda, *Tetrahedron*, 1985, **41**, 1555–1563.
89 D. Schröder, S. Shaik and H. Schwarz, *Acc. Chem. Res.*, 2000, **33**, 139–145.
90 R. Poli and J. N. Harvey, *Chem. Soc. Rev.*, 2003, **32**, 1–8.
91 P. Belanzoni, L. Bernasconi and E. J. Baerends, *J. Phys. Chem. A*, 2009, **113**, 11926–11937.
92 L. Bernasconi, P. Belanzoni and E. J. Baerends, *Phys. Chem. Chem. Phys.*, 2011, **13**, 15272–15282.
93 M. Gussoni, M. Rui and G. Zerbi, *J. Molec. Struct.*, 1998, **447**, 163–215.
94 T. N. Olney, N. Cann, G. Cooper and C. Brion, *Chem. Phys.*, 1997, **223**, 59–98.
95 N. Araújo, R. A. Mendes, L. Machado, M.-T. Lee and G. de Souza, *J. Electron Spectrosc. Relat. Phenom.*, 2021, **246**, 147029.

96 A. Bohn, C. Chinaux-Chaix, K. Cheaib, R. Guillot, C. Herrero, K. Sénéchal-David, J.-N. Rebilly and F. Banse, *Dalton Trans.*, 2019, **48**, 17045–17051.

97 W. Ye, D. M. Ho, S. Friedle, T. D. Palluccio and E. V. Rybak-Akimova, *Inorg. Chem.*, 2012, **51**, 5006–5021.